Effect of Microstructure on the Mechanical Properties and Fracture Toughness of API X65 Pipeline Steel in the Presence of Hydrogen

Meysam Ranjbar[1] · Reza Miresmaeili[1] ⬚ · Mohammad Reza Naimi-Jamal[2] · Majid Mirzaei[3]

Abstract

This study investigated the influence of microstructure on the mechanical properties and fracture toughness of API X65 pipeline steel in the presence of hydrogen. In this study, electrochemical method was used for hydrogen charging and indentation technique was applied to obtain the fracture toughness. The results showed that in the presence of hydrogen, elongation ($EL\%$), reduction of area (RA), ductile fracture percentage, and fracture toughness of all microstructures decreased. The microstructure of martensite (M) + bainite (B) + ferrite (F), had the highest hydrogen trapping and uptake (C_{app}) as 8.58×10^{-6} mol cm^{-3} and the lowest apparent hydrogen diffusivity (D_{app}) as 5.68×10^{-10} m^2 s^{-1}; thus, the maximum decrements of 33% in fracture toughness, 40% in ductile fracture percentage, 47% in RA, and 35% in EL% were observed. However, the microstructure of ferrite (F) + degenerated perlite (DP) + martensite-austenite micro constituent (M/A), where the lowest value of 5.85×10^{-6} mol cm^{-3} for C_{app} and the highest value of 8.5×10^{-10} m^2 s^{-1} for D_{app} had the minimum decrements as 2% in fracture toughness, 10% in ductile fracture percentage, 4% in RA, and 7% in El%. According to the obtained results, depending on the type of microstructures, hydrogen-induced work softening or hardening were observed by decreasing or increasing the yield stress respectively.

Keywords Microstructure · Fracture toughness · Indentation technique · Hydrogen permeability · Hydrogen enhanced softening and hardening

1 Introduction

Hydrogen embrittlement (HE) is one of major unexpected failure mechanisms in API pipeline steel. Wang [1] reported that local corrosion and cathodic protection can produce hydrogen atoms. Then, due to small atomic radius of hydrogen it can diffuse into the steel and dissolve at the interstitial sites, or be trapped at defect zones such as dislocations, grain boundaries, etc. [2]. The quantity of trapped and dissolved hydrogen in a material depends on the type of microstructure and the density of defects [1, 2]. Hejazi et al. [3] studied the influence of microstructure on the sensitivity of API X70 steel and showed that the trapping of hydrogen is highly dependent on the type of ferrite microstructure. Park et al. [4] reported that among ferrites, bainitic ferrite is the most effective microstructure on hydrogen trapping. On the other hand, other researchers found that the acicular ferrite trapped hydrogen more than ultrafine ferrite [5]. Lunarska et al. [6] investigated the hydrogen trapping behavior in various microstructures and concluded that hydrogen-trapping efficiency diminished as follows: martensite, bainite, fine

✉ Reza Miresmaeili
    miresmaeili@modares.ac.ir

    Meysam Ranjbar
    meysam.ranjbar@modares.ac.ir

    Mohammad Reza Naimi-Jamal
    naimi@iust.ac.ir

    Majid Mirzaei
    mmirzaei@modares.ac.ir

1   Department of Materials Engineering, Tarbiat Modares University, Jalal Ale Ahmad Highway, 14115-143, Tehran, Iran

2   Research Laboratory of Green Organic Synthesis and Polymers, Department of Chemistry, Iran University of Science and Technology, 16846-13114, Tehran, Iran

3   Department of Mechanical Engineering, Tarbiat Modares University, 14115-143, Tehran, Iran

perlite, coarse perlite, and secondary-phase particles. It was assumed that the segregated zones with martensite or bainite were harmful for hydrogen-embrittlement sensitivity. It was also reported that sensitivity of lower bainite to hydrogen embrittlement was lower than quenched and tempered martensite [5, 6]. Huang et al. [7] reported that microstructures including granular bainite (GB) containing M/A micro constituents increased sensitivity to hydrogen cracking.

The interaction of trapped and dissolved hydrogen with dislocations can affect mechanical properties especially fracture toughness. Fracture toughness can be defined as resistance of cracked material to the crack propagation [8]. ASTM E-399 standard suggests common test methods for measuring fracture toughness where in the presence of hydrogen, NACE TM 0177 standard is used. In all test methods, in addition to the difficult procedure of tests, pre-cracked samples with special dimensions are required thus making it difficult, expensive, and time-consuming. Over the past decades, many efforts have been made to develop simple and non-destructive test methods. Indentation method is usually used to measure hardness; Lawn et al. first proposed this technique to obtain fracture toughness in brittle materials in 1980 [9]. Afterward, studies were done to develop this technique for ductile materials [10–12]. Computer simulations results showed that under indentation tip similar to crack tip, the deformation field and the degree of stress constraint are the same. Meanwhile, many practical studies obtained fracture toughness by indentation technique and reported that there is good agreement (about 10% differences) in the results obtained by other common methods [8, 12, 13]. For example: Lee et al. [13] used both indentation and Crack Tip Opening Displacement (CTOD) tests four steels of ASME SA335 P12, API X65, ASME SA 106, API X70 and observed that indentation technique showed a good agreement with the results of CTOD tests. Min He et al. [14] used indentation and Compact Tension (CT) tests to obtain fracture toughness of AA 5052-O1 and SS302

stainless steel. They observed that the fracture toughness obtained by indentation tests had good conformity with the results of CT tests. Other studies also reported good agreements of indentation test results with common test methods [8, 15–17]. Thus, it seems that indentation method can be a suitable alternative technique to measuring fracture toughness in ductile materials.

So far, indentation method has not been used to measure the fracture toughness of ductile materials such as API steels in the presence of hydrogen. On the other hand, the contradictory results about microstructure effects on the mechanical properties in the presence of hydrogen in pipeline steels suggest the necessity of further research in this field. Thus, the aim of this work is to study the effect of microstructure on mechanical properties in the presence of hydrogen using indentation method to measure the fracture toughness. Hence, API X65, which is widely used in gas and oil transportation systems, was selected for this study.

2 Experimental Procedure

2.1 Sample Preparation

The chemical composition of API X65 steel is presented in Table 1. Different microstructures from as-received thermo mechanical API X65 steel in rolling direction were obtained under heat treatments. Table 2 reports the codes of the samples according to type of their heat treatments.

2.2 Microstructural Characterization

All specimens were ground up to 3000 grit paper and then mirror polished using 0.2 μm Al_2O_3 suspension. They were cleaned with acetone and etched with Nital 2%. Meanwhile, for more analysis, the samples were tint etched as follows: pre-etching by 4% picral (4 g picric acid in 100 mL ethanol)

Table 1 Chemical composition of API X65

Element	Fe	C	Mn	Si	Al	P	S	Ni	N	Sn	Mo	V	Nb	Ti	Co	Cr	B
wt%	Bal	0.1	1.45	0.2	0.035	0.02	0.005	0.004	0.003	0.002	0.04	0.069	0.054	0.041	0.002	0.04	0.001

Table 2 Heat treatment cycles

Sample code	Austenizing temperature (°C)	Austenizing time (min)	Cooling condition
TMCP	As-received	–	–
800 W	800	30	Water cooled
860 A	860	30	Air cooled
60 A	860	30	Quench in salt bath of 530 °C and held for 60 s and then Air cooled

for 60 s and then dipping in 10% sodium metabisulfite solution (10 g sodium metabisulfite in 100 mL distilled water) for 15 s [18]. The microstructures were characterized by both OM using OLYMPUS BX51M and SEM using a VEGAII TESCAN SEM at voltage of 20 kV. The volume percentage of all phases in the microstructures was obtained by MIP4 Students and MIP Cloud software.

2.3 Electrochemical Hydrogen Permeation Test

ISO 17081: 2004 E standard test method was used to measure the hydrogen permeability by Devanathan and Stachurski electrochemical cell [19]. Figure 1 displays the schematics of modified dual cell and all information about solutions, electrodes, etc. Note that ammonium thiocyanate (NH_4SCN) was used to increase hydrogen diffusion and hinder formation of hydrogen molecules. Specimens with thickness of 1 mm were prepared and then both sides of them were ground up 600 grit paper and cleaned with methanol. In the hydrogen detection side, in order to deposit a thickness of 100 nm of pd film, an electrochemical method was used. The coating bath was 2.54 g of $PdCl_2$ and 500 ml of 28% aqueous ammonia solution and a galvanostatic current density of 2.83 mA cm^{-2} was cathodically applied for 2 min [20]. The cleaned specimen with exposed area of π cm^2 was placed between two electrochemical cells. To start the test, at first the detection side was filled and then + 250 mV (SCE) was applied while anodic current was monitored until reaching a stable background current. Next, the charging cell was filled and then a current density of 5 mA/cm^2 was applied using Dazheng DC power supply model ps-3050. The extraction flux of hydrogen is proportional to the current density (i) on the detection side. Until reaching a steady state, the changes

in i with time were monitored**.** The hydrogen permeation rate $J_{ss}.L$ (mol cm^{-1} s^{-1}) is defined as [21–23]:

$$J_{SS}L = \frac{i_{SS}L}{2F} \tag{1}$$

In the above equation, i_{ss} represents the current density at steady state, L is specimen thickness, and Faraday constant is shown by F. The effective hydrogen diffusivity, D_{eff} (cm^2 s^{-1}), using time lag method, is defined as [21–23]:

$$D_{app} = \frac{L^2}{6t_L} \tag{2}$$

where t_L (s) is the lag time, known as 0.63 steady state time. The apparent hydrogen solubility C_{app} (mol cm^{-3}) is described by [21–23]:

$$C_{app} = \frac{J_{SS}L}{D_{app}} \tag{3}$$

Hydrogen trap density could be estimated by the following equation [23]:
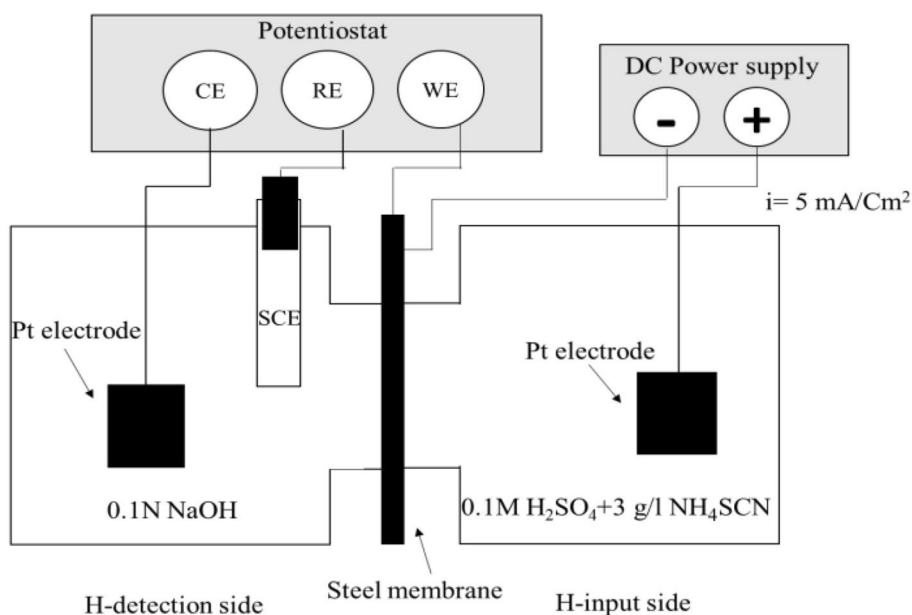
$$N_t = \frac{C_{app}}{3}\left(\frac{D_L}{D_{app}} - 1\right) \tag{4}$$

where N_t is the hydrogen trapping density per volume, D_L denotes hydrogen diffusion coefficient in ferrite and equals to 7.2×10^{-9} m^2 S^{-1}.

2.4 Tensile Test

In order to investigate the hydrogen effect on mechanical properties of the samples, tensile tests were performed on

Fig. 1 Schematic of Devanathan-stuchurski cell

the reference (not-charged) as well as pre-charged samples. In order to perform hydrogen pre-charging operation, after grinding the sample surfaces by 60 to 2000 Sic papers, in the presence of a 316 stainless steel as the cathode, they were pre- charged for 12 h in the charging solution (mentioned in Sect. 2.3) with an applied current density of 5 mA/cm^2. In-situ charging operation was also performed during tensile test. For this purpose, a special cell and a special tensile jaw which was resistant against corrosion and hydrogen embrittlement were designed and fabricated. During tensile tests, the samples were exposed to the same solution and charging conditions with the pre-charging process. The tensile test was performed by Instron equipment with a maximum applied load of 20 tons and tension speed of 1 mm/min on all samples. Further, all test conditions were performed three times with the average of results reported. The prepared samples for tensile tests were the same for both charged and reference (non-charged) conditions and they were prepared in miniature with a gauge length of 12.5, thickness of 4.7, and width of 3 mm.

2.5 Fracture Toughness Obtained by Indentation Test

Firstly, 5 specimens with the length and width of 30 mm and thickness of 1 mm were prepared from the samples. Once ground, the specimen surfaces were mirror polished by alumina powder solution. In the next stage, one side of the samples was covered with a specific adhesive and the other side was pre-charged as mentioned in Sect. 2.4. After pre-charging, micro-indentation test was performed on the reference and pre-charged samples. A constant displacement method was used with 5 indentation depths from 20 to 100 μm with intervals of 20 μm. The loading and unloading rates of indentation test were 5 μm/s. Each indentation test was performed three times with the average of results reported. The output of indentation test is load (F)-penetration depth (h_p) diagram. Plastic deformation energy or indentation energy (G_{IE}) is the definite integral of P-h_p. Imaginary fracture occurs when indentation energy reaches a critical value (G_{IEF}) at h_p^* and can be expressed as Eq. 5: [24–35]:

$$G_{IEF} = \int_0^{h_p^*} F(h_p)dh_p = \int_0^{h_p^*} \frac{F(h_p)}{A_p(h_p)}dh_p \qquad (5)$$

In the above equation, P is the pressure of indentation, F denotes indentation load, and A_p shows the plastic area of indentation and expressed as [24–35]:

$$A_P = 23.75h_p^2 \qquad (6)$$

G_{IEF} can be related to strain energy density by the following equation:

$$G_{IEF} = \frac{S_{cr}(1 - \vartheta)}{(1 - 2\vartheta)} \qquad (7)$$

In Eq. 7, S represents the strain energy density and ϑ is the Poisson ratio of the material and assumed 0.3. While, S reaches to a it's critical value (S_{cr}) it could be considered as a crack extension energy. S_{cr} signals the fracture toughness and its relationship with K_{IC} is described by the following equation [24–35]:

$$K_{IC} = \sqrt{\frac{2ES_{Cr}}{(1 + \vartheta)(1 - 2\vartheta)}} \qquad (8)$$

As shown earlier, in order to calculate the fracture toughness, it is necessary to obtain the critical indentation depth (h_p^*). Thus, it reduced elastic modulus (E_r) and effective material elastic modulus ($E^{\sim}$) should be defined, according to the following equations [24–35]:

$$A_c = 24.504h_c^2 \qquad (9)$$

$$E_r = \frac{k.\sqrt{\pi}}{2\beta.\sqrt{A_c}} \qquad (10)$$

$$E^{\sim} = \frac{(1 - \vartheta^2)}{\left(\frac{1}{E_r} - \frac{1-\vartheta_i^2}{E_i}\right)} \qquad (11)$$

In the above equations, h_c shows elastic depth of contact, E_i denotes the elastic modulus of indentation tip (900 GPa), and ϑ_i denotes the Poisson's ratio of indenter (0.02). A_c is the area of contact and K shows the stiffness in unloading. β is a correction factor induced by loss of axial polarity and set as 1.0124 for Vickers indenter [24–35]. Having calculated $E^{\sim}$ at various h_c, the equation between $E^{\sim}$ and h_p can be extracted. ln $E^{\sim}$-ln h_p curve shows an almost linear trend and its equation can be obtained easily. The effective elastic module at the imaginary fracture initiation point ($E_{min}^{\sim}$) related to the elastic modulus of material (E ≈ 210 GPa) can be obtained by the following equation [24–35]:

$$E_{min}^{\sim} = 0.51E \qquad (12)$$

When $E_{min}^{\sim}$ is obtained by Eq. 12, then h_p^* can be identified by the linear equation observed between ln $E^{\sim}$ and ln h_p. Now by replacing h_p^* in Eq. 6, G_{IEF} can be obtained and then S_{cr} will be calculated by Eq. 8. Finally, the fracture toughness will be obtained by Eq. 9.

3 Results

3.1 Microstructures

OM images of tinted etch of 800 W, 860 A, 60 A, and TMCP samples are shown in Fig. 2. This tint etchant shows martensite in brown, bainite in blue, as well as ferrite and retained austenite in white [18]. As can be seen, only in 800 W sample brown color which represents martensite was observed. Also, only in 60 A and 800 W samples, bainitic microstructure with blue color were observed. By using MIP4 image processing software, the percentages of colored phases of martensite and bainite as well as white zones were calculated with the results shown in Table 3. For more accuracy, at least 10 images of each sample were analyzed. The white zones in the images of Fig. 2 can represent two phases of ferrite and retained austenite, where to measure the percentage of retained austenite, XRD method was used. In XRD patterns, austenite phase peaks were not observed. Thus, it can be concluded that the white zones in Fig. 2 are ferrite [36–41]. On the other hand, dark zones can be observed in images of 2-a–c. In

Table 3 Phase percent of samples

Sample %volumetric	F	M	B	MA	DP
TMCP	87 ± 3	–	–	3 ± 0.5	10 ± 1
800 W	50 ± 5	40 ± 3	10 ± 1	–	–
860 A	92 ± 2	–	–	3 ± 1	5 ± 1
60 A	57 ± 1	–	35 ± 1	8 ± 1	

Ferrite (F), Martensite (M), Bainite (B), Martensite-Austenite (MA), Degenerated Perlite (DP)

order to recognize and calculate the volume percentage of these zones, higher magnification images were taken by SEM. Figure 3 displays the SEM images. As can be seen in the images of 60 A, 860 A and TMCP samples dark zones could be identified as degenerated perlite (DP) and martensite-austenite (M/A) micro constituents. Meanwhile, as shown in Fig. 2a, b the carbides in ferrite grains in 860 A sample is coarser than in TMCP. Also, the M/A micro constituents in 860 A sample had Island-shape while in TMCP and 60 A samples, the morphology changed to strips around ferrite grains. As can be seen in Fig. 3d, in
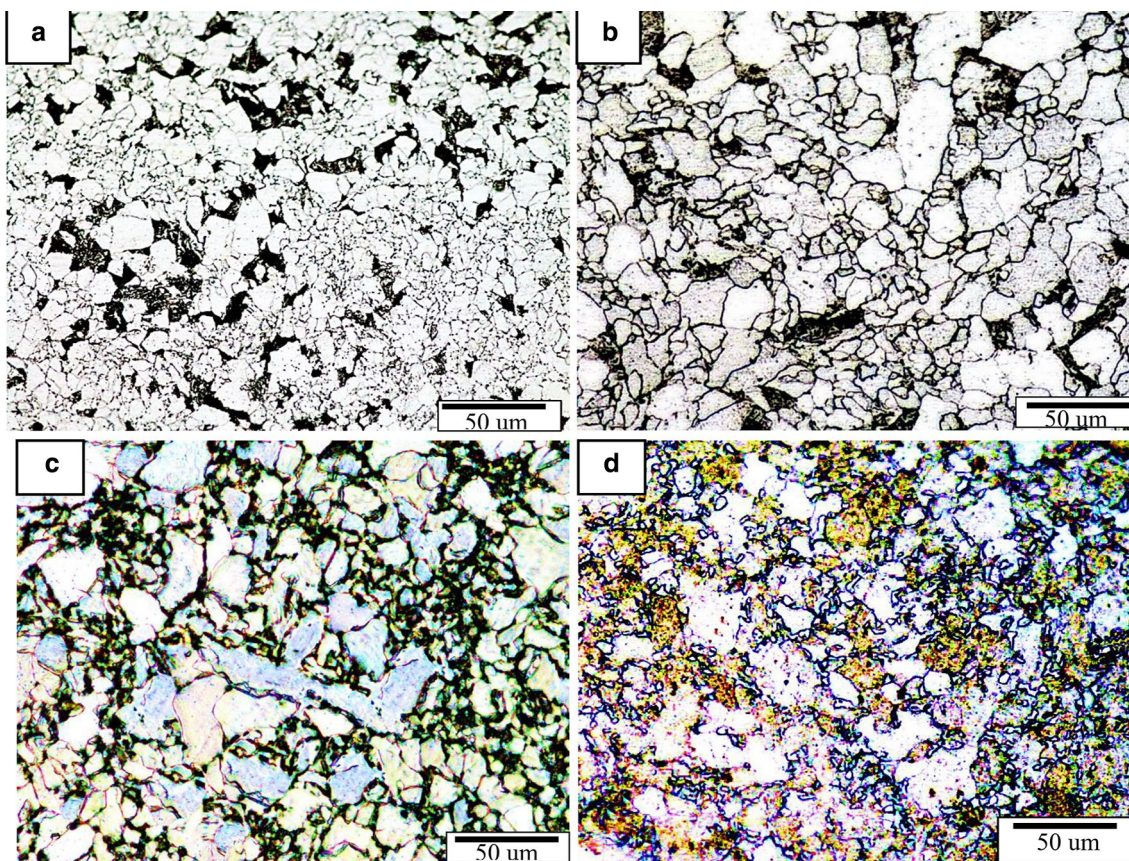

Fig. 2 OM micrograph of Etched microstructure by etchant No. 2. **a** TMCP, **b** 860 A, **c** 60 A, **d** 800 W
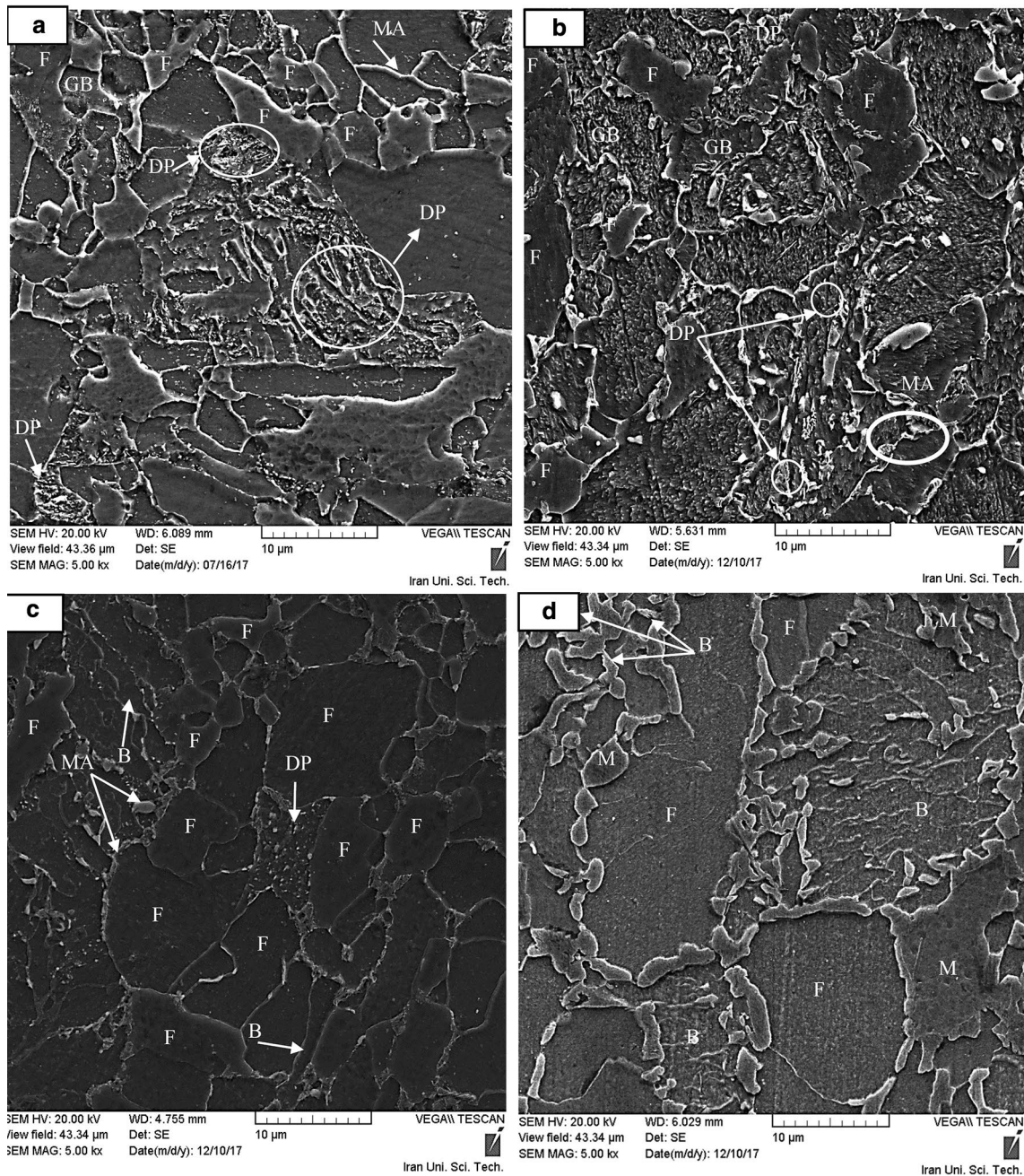
Fig. 3 SEM images of **a** TMCP, **b** 860 A, **c** 60 A, **d** 800 W

the 800 W sample, martensite (M) packets, bainite (B) laths and ferrite (F) grains were clearly marked in the microstructure.

3.2 Hydrogen Permeation

Figure 4 reveals the normalized diagram of hydrogen permeation vs. a dimensionless time coefficient [42, 43]. Hydrogen permeation (J) is normalized by dividing to the

super saturation permeability (J_{SS}) and dimensionless time is also calculated by Eq. 13 [43]:

$$\tau = \frac{D_L.t}{L^2} \tag{13}$$

In the above equation, D_L means coefficient of hydrogen diffusion in ferrite with value of 7.2×10^{-9} m^2/s at room temperature [44]; t denotes time (seconds), and L is the sample thickness (m). As observed in Fig. 4, in all of
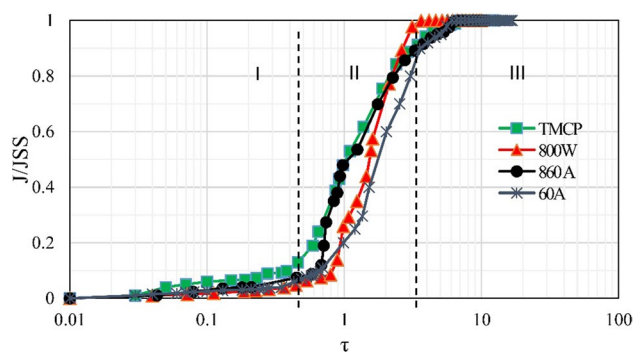
Fig. 4 J/J_{SS}-τ curves of samples

the samples, the normalized permeability has increased with time, and past a transient zone, it reaches a saturation state. Also, no significant difference can be observed between the behaviors of different samples. As can be seen in Fig. 4, the diagrams are divided into three zones. In zone I, atomic hydrogen starts to dissolve in the lattice and gets entrapped in reversible and irreversible traps. In zone II, called the transient zone, hydrogen is dissolved and trapped with a sharper rate. In zone III, the sample get saturated by the dissolved and trapped hydrogen. The start times of zones III, II, and the slope of the transient zone are the important points [19–23]. The shortest start time of transient zone is 46 s related to TMCP sample, followed by 57 s, 64 s and 79 s related to 860 A, 60 A, and 800 W samples respectively. The slope of transient zone (II) in 800 W is equal to 0.3, 0.18 for 60 A, and 0.1 in TMCP as well as 860 A samples. The shortest start time of saturation is 778 s and related to 800 W. The maximum saturation time is 1877s in 60 A. Additionally, saturation times in TMCP and 860 A are 1745 s and 1670 s respectively. The values of C_{app} (the dissolved hydrogen in the lattice and reversible traps), D_{app} (apparent diffusion coefficient of dissolved and trapped hydrogen in reversible traps) and N_t (density of traps) using the explained procedure described in Sects. 2–3 were calculated with the results shown in Table 4. The general belief is that by increasing C_{app}, as well as decreasing D_{app} and $J_{SS}.L$, more hydrogen is trapped in steel [45, 46]. Studies found that hydrogen diffusivity in ferrite was in the order of 10^{-8} m^2 s^{-1} [44, 45],

while in this study it is lower about 10^{-2} m^2 s^{-1}. Apparently, the defects such as inclusions, grain boundaries, and precipitates can function as hydrogen trapping zones and reduce hydrogen diffusivity [45]. The values observed in Table 4 are similar to the results reported in various studies for pipeline steels including API X65 steel [46–49].

3.3 Mechanical Properties and Fracture Toughness Parameter

The stress–strain diagrams of the reference and charged samples are presented in Fig. 5. Table 5 reports the extracted values of yield strength (Ys), ultimate tensile strength (UTS), elongation (EL), reduction of area (RA), and Ln (A_0/A_f) (A_0 is the initial cross section equal to 14.1 mm^2, and A_f is the final cross section). In Table 5, the TMCP sample with a microstructure of F + DP + MA has a yield stress of about 355 MPa and UTS of about 560 MPa. In the 800 W sample, with a microstructure of F + M + B due to the presence of M + B laths, the yield stress and UTS increased by about 20% and 30% respectively while the elongation decreased from 52 to 42%. The sample of 860 A with the microstructure of F + DP + MA in comparison to TMCP showed a 15% decrease in the yield strength, 18% decrease in UTS, and 13% increase in elongation due to the decrement of DP percent and absence of thermomechanical effects. The 60 A sample with the microstructure of F + B + MA had an increment of about 6% in the yield stress and decrement of about 6% in the elongation than TMCP. The increase in the percentage of brittle M/A micro constituents as well as the presence of B can result in higher yield stress and lower elongation in 60 A than TMCP. On the other hand, in the case of UTS, no considerable change is observed.

By pre-charging operation as well as in-situ charging, the values of Ys, UTS, and %El changed. Table 6 reports the changes induced by hydrogen charging. As can be seen in Table 6, in all samples except 800 W, Ys and UTS increased by hydrogen charging. In other words, for all samples except 800 W, due to elevation of Ys, hardening is observed. Based on Table 6, hydrogen charging operation resulted in diminished ductile fracture percentage, El, and RA values in all samples. The maximum decline in the ductile fracture percentage, RA, and El has been equal to 40%, 47% and 35%

Table 4 Data's obtained by devanatan-stuchurski cell	800 W	860 A	60 A	TMCP
$I_{SS} \times 10^{-6}$ (A)	506 ± 8	398 ± 6	406 ± 4	480 ± 5
$J_{SS}.L \times 10^{-9}$ (mol m^{-1} S^{-1})	6.27 ± 0.1	4.926 ± 0.1	5.07 ± 0.1	5.94 ± 0.1
$C_{app} \times 10^{-6}$ (mol/Cm^3)	10.99 ± 0.05	5.85 ± 0.03	7.87 ± 0.03	6.78 ± 0.03
$D_{app} \times 10^{-10}$ (m^2 S^{-1})	5.68 ± 0.11	8.39 ± 0.2	6.47 ± 0.18	8.67 ± 0.1
$N_T \times 10^{25}$ (mol Cm^{-3})	2.67 ± 0.14	0.924 ± 0.04	1.65 ± 0.11	1.04 ± 0.05
t (s)	165 ± 3	111.74 ± 2	145.643 ± 4	108.13 ± 2

Fig. 5 Stress–strain curves of charged and reference samples of: **a** 800 W, **b** 860 A, **c** 60 A and **d** TMCP (Added symbol -c at the end of sample codes means charged)
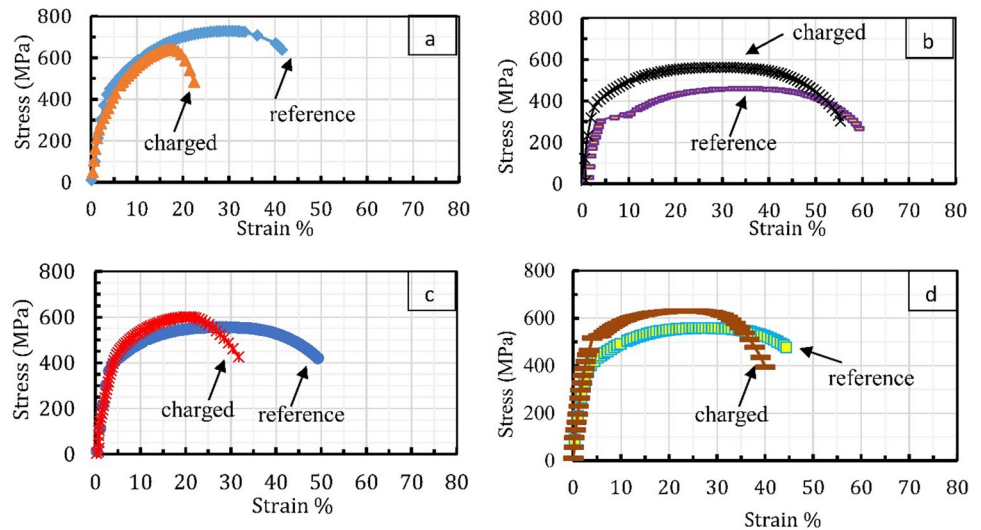

Table 5 Results of stress–strain curves of all samples in the presence and absence of hydrogen

	800 W	800 W-C	860 A	860 A-C	60 A	60 A-C	TMCP	TMCP-C
YS (MPa)	426 ± 13	283 ± 23	300 ± 1	380 ± 2	378 ± 1	444 ± 2	355 ± 2	452 ± 2
UTS (MPa)	729 ± 23	684.5 ± 41.5	458 ± 3	562 ± 2	555 ± 3	609 ± 9	560 ± 6	634 ± 3
Elongation (El%)	42 ± 1.5	22 ± 2.5	59.4 ± 1.6	55 ± 1	49 ± 2	32 ± 1.2	52 ± 1	45 ± 1.5
Reduction of area (RA)	0.45	0.3	0.73	0.7	0.6	0.47	0.65	0.57
Ln(A0/A)	0.6	0.34	1.32	1.211	0.94	0.64	1.05	0.85
Ductile fracture percent	30%	18%	66%	52%	34%	24%	60%	45%

*Added symbol –c at the end of sample codes means charged

Table 6 Change in the values of obtained results of stress–strain curves due to presence of hydrogen

	800 W-C Vs. 800 W	860 A-C Vs. 860 A	60 A-C Vs. 60 A	TMCP-C Vs. TMCP
$\Delta Y_S\%$	-33.5%	26%	17.4%	27%
$\Delta UTS\%$	-6%	22%	9%	13%
$\Delta El\%$	-47%	-7%	-35%	-13%
$\Delta RA\%$	-35%	-4%	-22%	-11%

$\Delta Y_S\% = \frac{Y_{SC}-Y_{SR}}{Y_{SR}} \times 100$, $\Delta UTS\% = \frac{UTS_C-UTS_R}{UTS_R} \times 100$, $\Delta El\% = \frac{El_C-El_R}{El_R} \times 100$,$\Delta RA\% = \frac{RA_C-RA_0}{RA_0} \times 100$

*Added symbol –c at the end of sample codes means charged

respectively belonging to the 800 W sample. The 860 A sample with 10% decrease in the ductile fracture percentage, 7% decrease in elongation, and 4% reduction in area has had the minimum decrement. Further, 60 A and TMCP Samples had 30% and 25% decrease in ductile fracture percentage, 35% and 13% decrease in elongation, and 22% and 11% in reduction of area respectively. It seems that by increasing

D_{app} and reducing C_{app}, the extent of reduction in the fracture percentage, RA, and El diminished.

Figure 6 reveals the SEM images of the fracture surfaces of charged and reference samples at low magnification. Quasi-cleavage (QC) and ductile fracture areas have been marked on these images. Through dividing the areas of the ductile fractured region by the total area, the percentage of ductile fracture could be calculated. The calculation results are presented in Table 5. As can be seen in Table 5, due to the presence of hydrogen, the percentage of ductile fracture decreased in all samples.

For further studies on fracture surfaces, SEM images with higher magnification were taken and shown in Fig. 7. In Fig. 7a, c, e, g (reference samples), the features of ductile fracture such as dimples are observed. In Fig. 7b, d, f, h (charged samples), in comparison to reference samples (Fig. 7a, c, e, g) it can be stated that: (1) the volume fraction of dimples decreased (2) dimensions of dimples shrank and (3) the fracture surfaces became smoother.

Based on the observations of Fig. 7, in the presence of hydrogen, volume fraction and the length and width of dimples decreased at fracture surfaces. Table 7 reports the

Fig. 6 Low magnification SEM images of fractured samples of: **a** 800 W, **b** 800 W-C, **c** A860, **d** A860-C, **e** 60 A, **f** 60 A-C, **g** TMCP, **h** TMCP-C
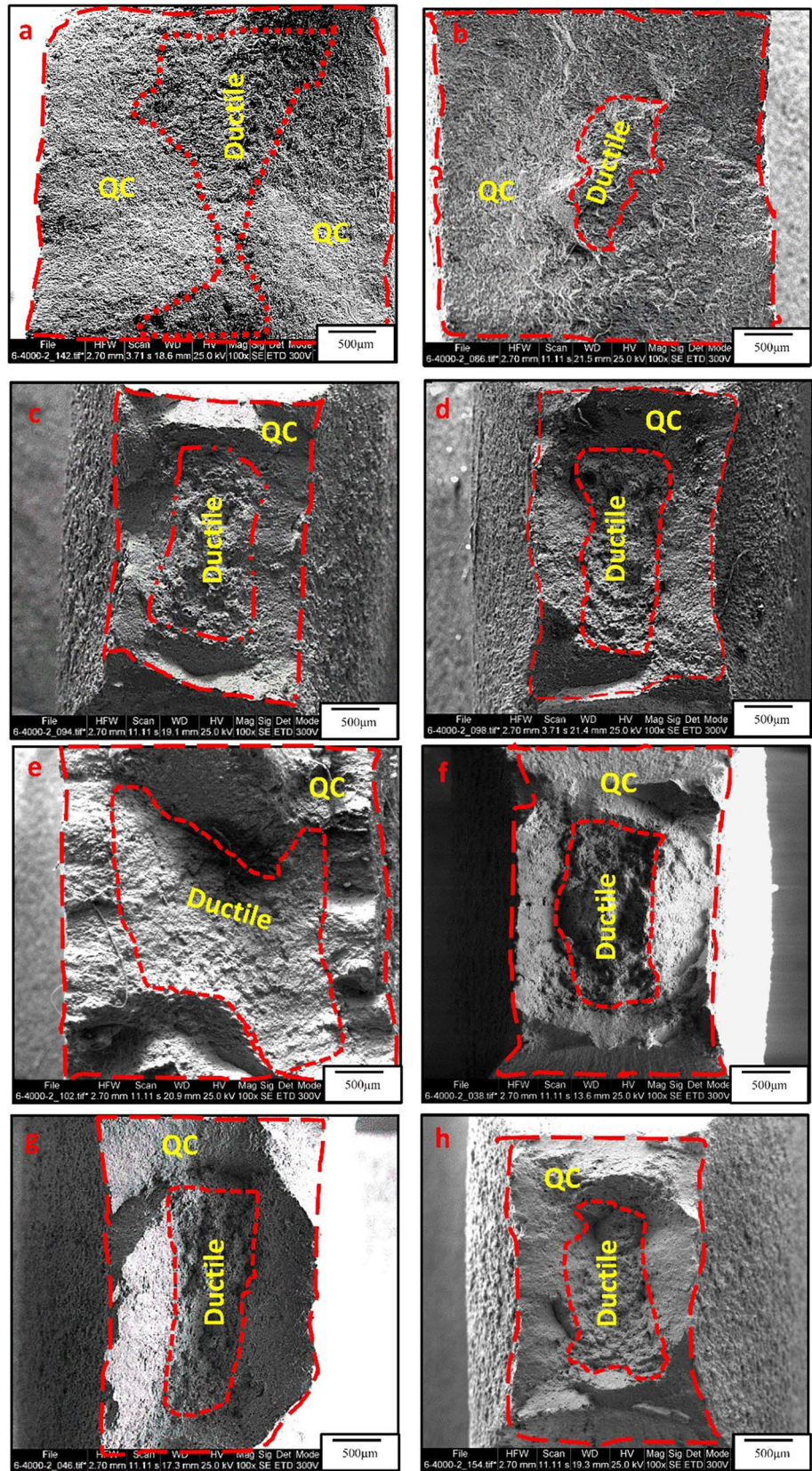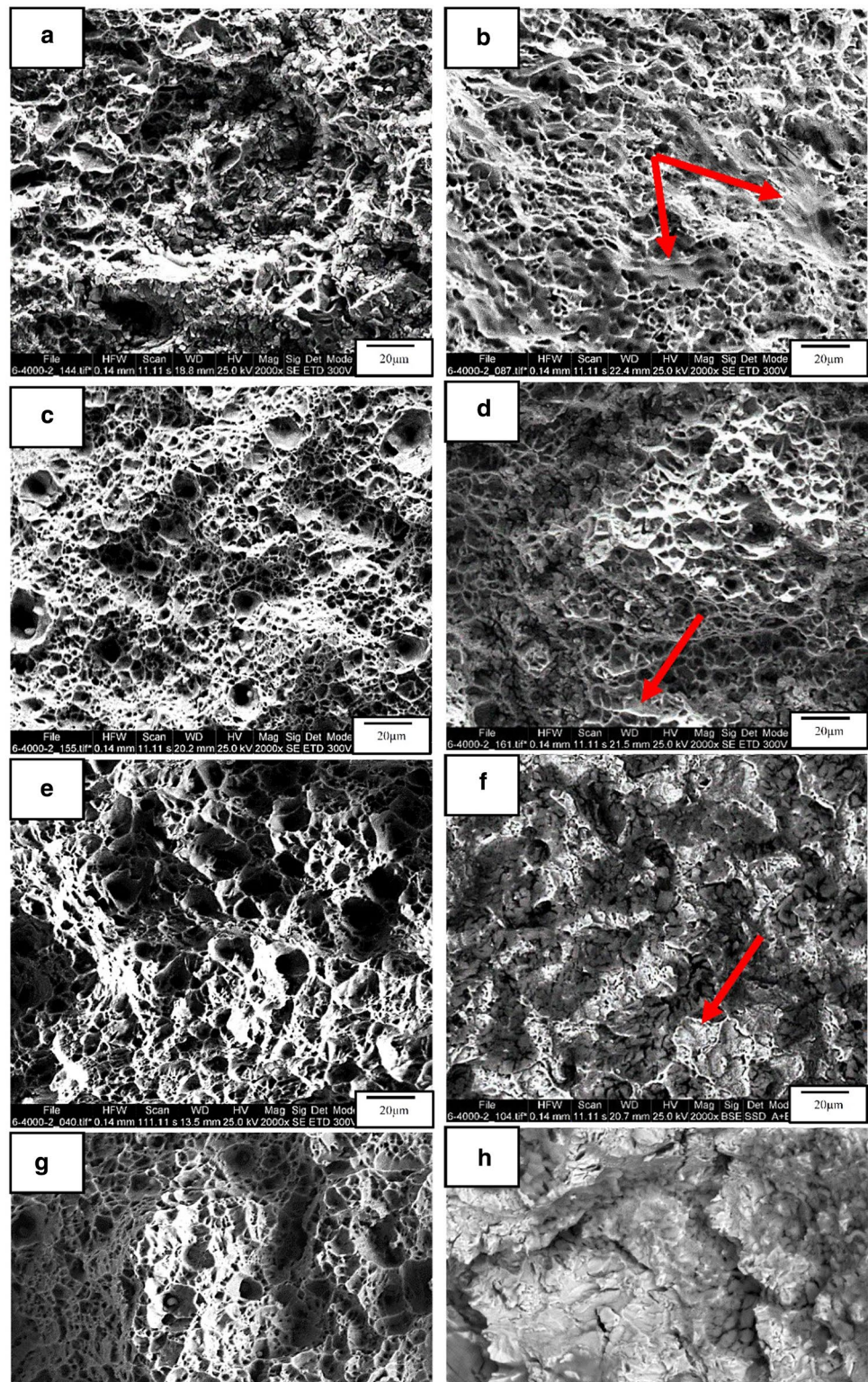
Fig. 7 High magnification SEM images of fractured samples of: **a** 800 W, **b** 800 W-C, **c** A860, **d** A860-C, **e** 60 A, **f** 60 A-C, **g** TMCP, **h** TMCP-C

average measured length and width of the dimples obtained by MIP4 software.

Figure 8a–h reveals the load–displacement diagram of the samples in the indentation test. In The fracture toughness was calculated as described in Sect. 2–5. Figure 9 indicates Ln (Ẽ)-Ln h diagrams of samples. The critical depth (h_p^*) where Ẽ reached the critical value of 109.2 GPa was obtained through extrapolation. Figure 10 shows the F-h_p diagram for all charged and reference samples. As can be observed in all diagrams, the equations of force and

Table 7 Measured widths and lengths of dimples

Sample	Length (µm)	Width (µm)
800w	3 ± 0.2	1.8 ± 0.15
800 W-C	1 ± 0.05	0.5 ± 0.02
860 A	5 ± 0.12	3 ± 0.1
860 A-C	5 ± 0.3	2 ± 0.1
60 A	5 ± 0.2	3 ± 0.15
60 A-C	4 ± 0.11	2 ± 0.1
TMCP	5 ± 0.18	3 ± 0.2
TMCP-C	3 ± 0.23	1.7 ± 0.1

*Added symbol -c at the end of sample codes means charged

indentation depth were extracted. After obtaining the force equation and (h_p^*), the value of fracture energy (G), and then, the value of fracture toughness (K_{IC}) can be calculated.

Figure 11 depicts the columnar diagram of K_{IC} and G values of all charged and reference samples. As could be seen in Fig. 11, the G values for references samples are within the range of 120–153 kJ m^{-2}. Siahpour et al. [50] measured fracture energy of API X65 by CTOD and reported that the obtained G was within the range of 118–154 kJ m^{-2}, which was in good agreement with the G values obtained in all reference samples in this study. On the other hand, the G values for charged samples lie within the range of 60–150 kJ m^{-2} in
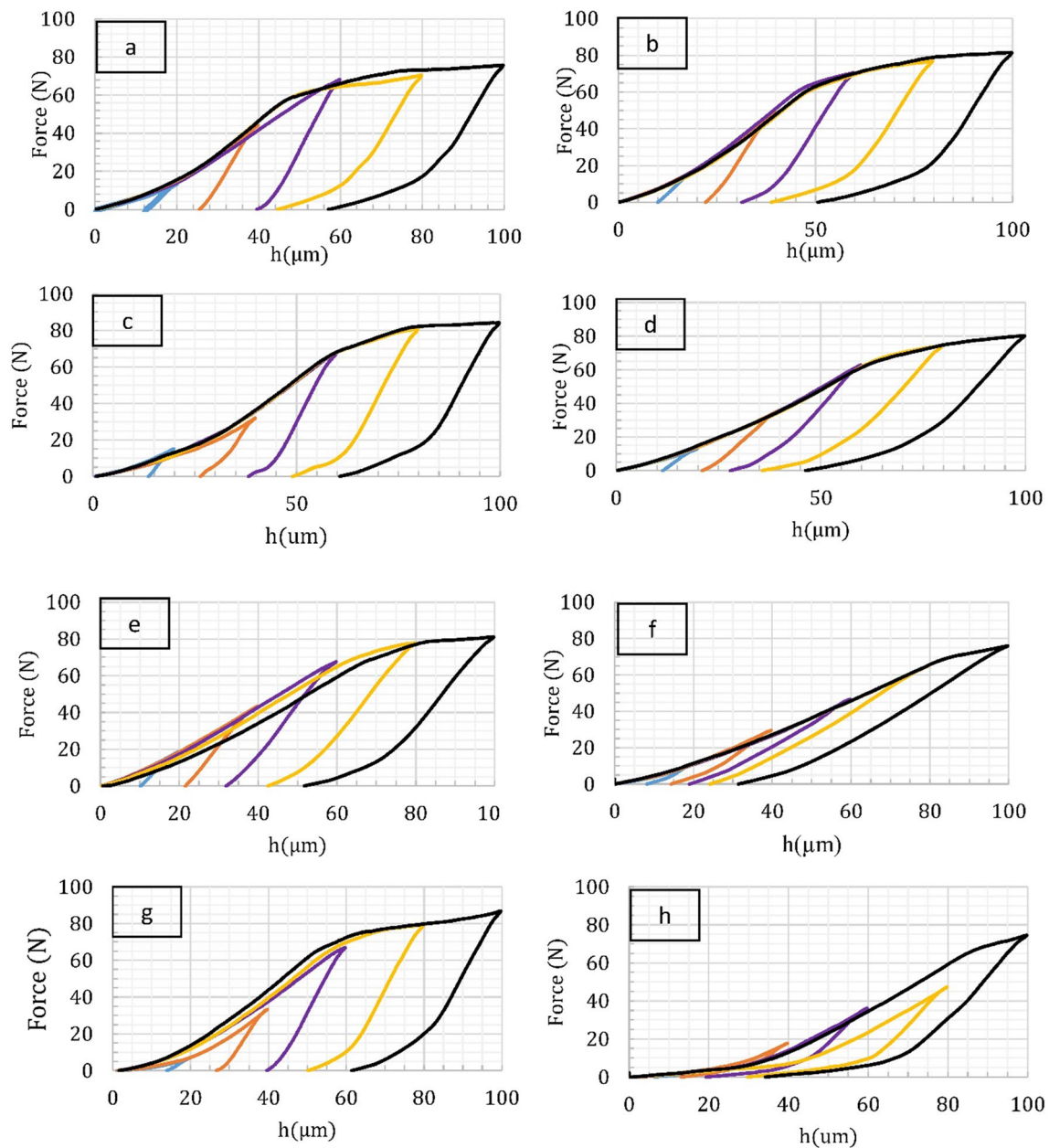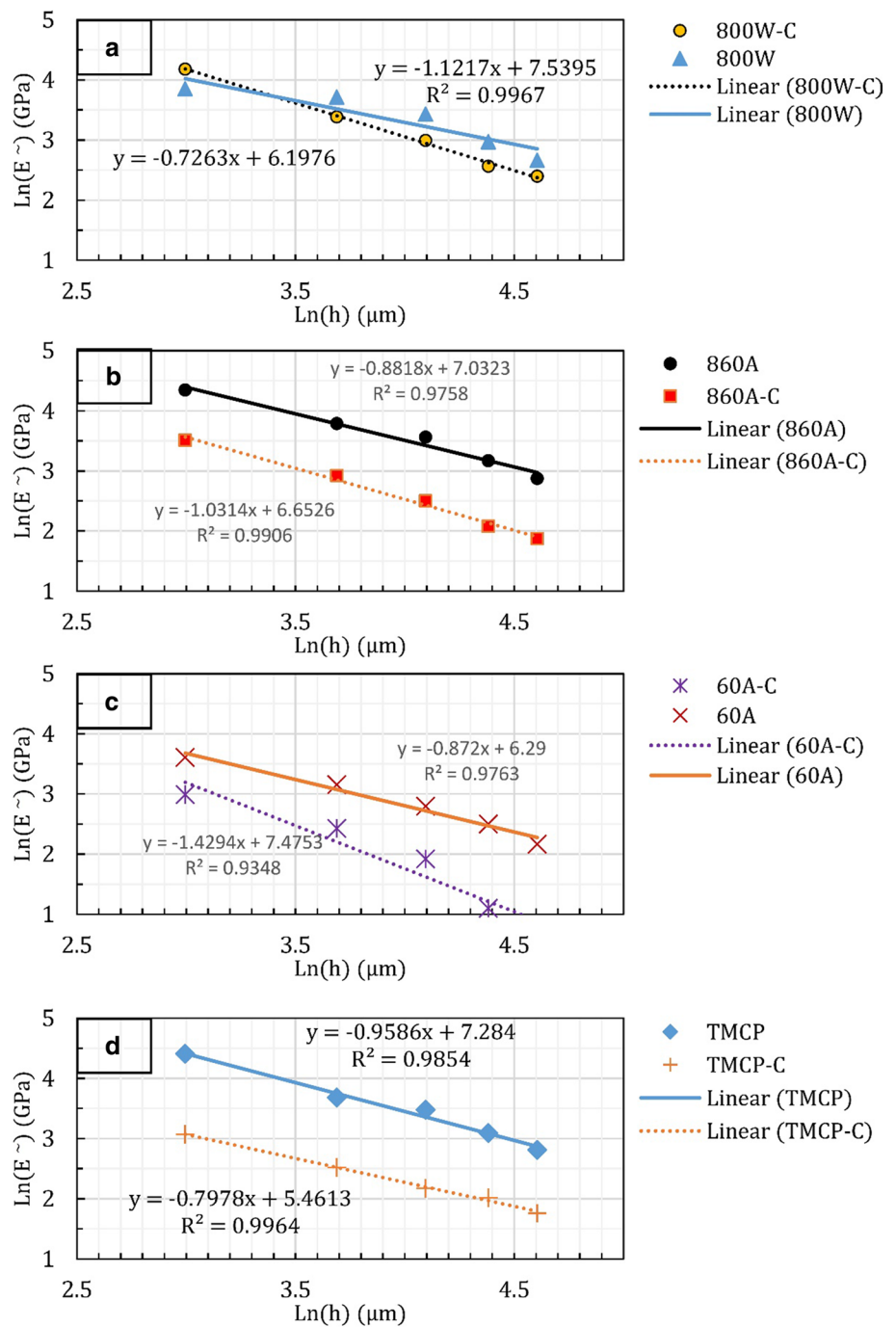

Fig. 8 Load–displacement curves of samples: **a** 800 W, **b** 800 W-C, **c** 860 A, **d** 860 A-C, **e** 60 A, **f** 60 A-C, **g** TMCP, **h** TMCP-C

Fig. 9 Ln (E˜)-Ln (h) curves of samples: **a** 800 W, 800 W-C, **b** 860 A, 860 A-C, **c** 60 A, 60A-C, **d** TMCP, TMCP-C

this investigation which are in good agreement with the values obtained by CTOD methods for measuring fracture energies of hydrogen charged API pipeline steels in other studies [1, 51, 52]. Figure 11 also indicates that by performing hydrogen pre- charging, in all samples, the values of K_{IC} and G have declined. The maximum values of K_{IC} and G belong to TMCP-C with the minimum values of K_{IC} and G being related to 800 W-C. Figure 12 presents the percentage of changes in K_{IC} and G values for all samples through the hydrogen charging operation. As can be seen, the maximum decline in the toughness and fracture energy such as elongation and ductile fracture percentage belongs to 800 W, followed by 60 A, TMCP, and finally 60 A, respectively.

Fig. 10 F–h curves of samples: **a** 800 W, 800 W-C, **b** 860 A, 860 A-C, **c** 60 A, 60 A-C, **d** TMCP, TMCP-C
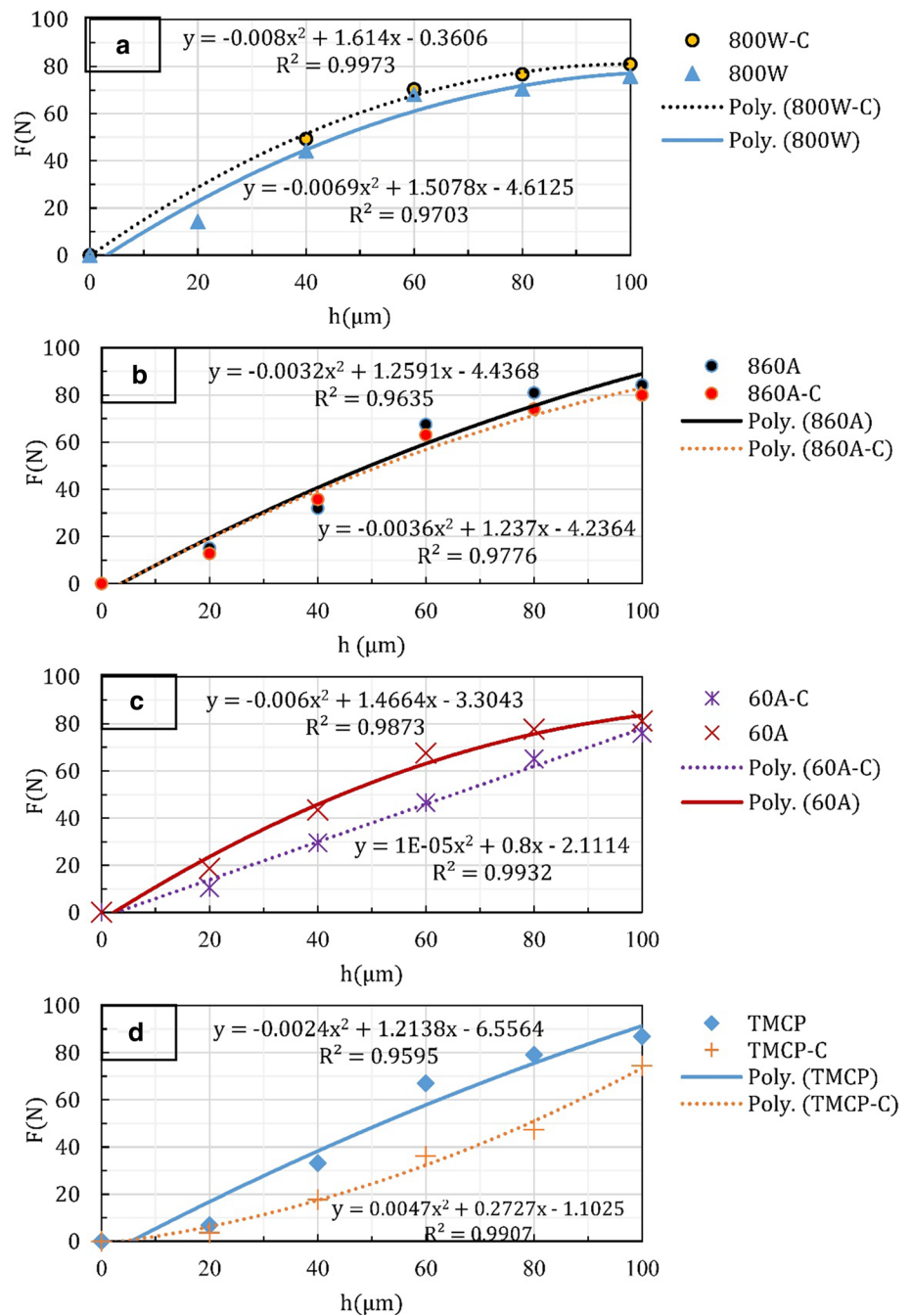
4 Discussion

4.1 Effect of Microstructure on Hydrogen Permeability

Hydrogen trapping in steel is a function of two parameters: (1) hydrogen concentration on the steel surface, (2) microstructural parameters such as type and volume percentage of phases, precipitations, and inclusions [45]. Hydrogen reaction with trapping zones is the basis for various mathematical models. In short, hydrogen trapping depends on the

number of traps and the hydrogen bonding energy with traps [53–61]. Generally, two types of reversible and irreversible traps have been recognized according to bonding energy with hydrogen [55–61]. Unlike reversible traps, irreversible traps do not release hydrogen at room or low temperatures due to higher bonding energy.

A more comprehensive categorization on traps based on the bonding energies with hydrogen introduces 3 types of weak, moderate, and strong traps [55–61]. In weak traps such as dislocations, fine precipitations, dissolved chromium, and molybdenum, the bonding energy is about 20 kJ/

Fig. 11 Fracture toughness and fracture energy of charged and uncharged samples
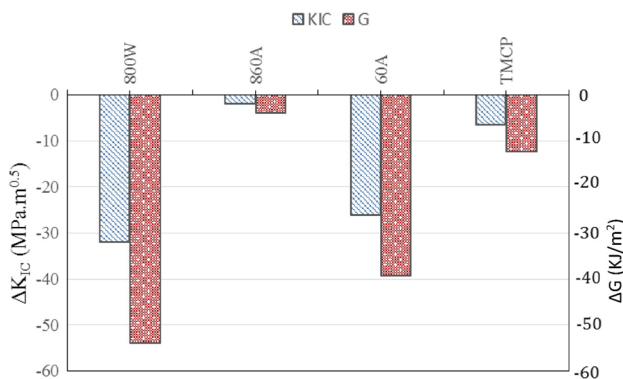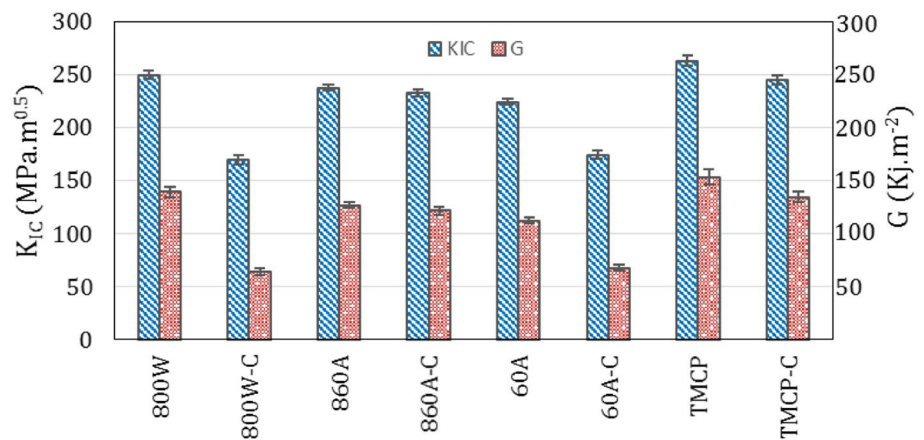

Fig. 12 Column diagram of change in fracture toughness and fracture energy percent of samples

mol, while in moderate traps such as martensite laths and primary austenite grain boundaries, the bonding energy is approximately 50 kJ/mol. Finally, in strong traps such as inclusions, spherical, and fine precipitations or impurity segregation, the bonding energy is about 100–120 kJ/mol.

Studies have shown that depending on the type of carbides, dissolving temperature lies within the range of 900–1150 °C [62, 63]. As austenitizing temperatures were 800 °C and 860 °C in this study, it is clear that no carbides dissolved due to heat treatments. Thus, changes in the diffusion coefficient, solubility, and density of traps could only be due to the type of microstructures formed.

As could be seen in Table 4, the maximum C_{app} and N_t as well as the minimum of D_{app} belong to 800 W. These can be attributed to: (1) high dislocation density in B + M microstructure, (2) the lath morphology of B and M and (3) higher point defects due to a higher cooling rate. Studies have found that the microstructure of quenched martensite had the minimum diffusion coefficient in comparison to other microstructures such as B or F/P [45–47]. However, 860 A has the minimum C_{app} and N_t. The microstructure of 860 A sample is mainly composed of F with large grain size which could result in low dislocation density as well as low area of grain boundaries. Thus, the density of reversible traps diminished and resulted in the minimum values of C_{app} and N_t in 860 A. Asher and Singh examined the hydrogen permeation behavior of APIX65 steel with abnormally high carbon of about 0.25% which was close to the final limit of API 5L carbon. They reported that coarse ferrite-perlite microstructure had the minimum C_{app} [64]. Further, in the comparison between TMCP and 860 A, it can be concluded that D_{app} and N_t are close, while, C_{app} in TMCP was about 14% higher than 860 A. In the microstructure of both samples, F was observed as the main phase along with MA + DP. In TMCP, the percentage of DP is two times of it in 860 A, that can be resulted in higher interfaces between ferrite and distributed carbides and could result in more reversible traps and, thus, C_{app} of TMCP was higher.

The comparison between the microstructures of TMCP and 60 A samples showed that the percentage of M/A in 60 A was about 1.65 times higher than in TMCP and also in 60 A sample against TMCP, bainite is present in the microstructure. In 60 A, D_{app} was about 25% lower, C_{app} was about 17%, and N_t was about 58% higher than in TMCP. The increase in the percentage of hard and brittle M/A phase and the presence of B in 60 A could result in enhanced dislocation density and thus more reversible traps which could result in an increase in the trapped hydrogen.

When comparing 60 A and 860 A samples, with increasing the volume percentages of M/A in 60 A and the presence of B as about 35% in this sample, D_{app} dropped by approximately 23% and C_{app} increased by about 35%. On the other hand, a considerable increment of 80% was observed in the trap density. Elevation of the dislocation density due to B laths and M/A constituent percentage could result in increasing hydrogen trapping; thus, C_{app} and N_t increased while D_{app} decreased in 60 A.

4.2 Effect of Hydrogen on Mechanical Properties and Fracture Toughness Parameter

Table 6 shows a decrement of − 33.5% in yield stress of 800 W due to hydrogen charging. Further, based on the results of Table 5, yield stress in 800 W-C sample is the lowest. As mentioned above, dislocation is one of the reversible traps in steels. It was reported that at room temperature, the majority of deformation occurred through screw dislocations [65]. The presence of hydrogen could lead to diminished required energy for kink formation on dislocations [65]. On the other hand it was reported that due to the elastic shielding effect of hydrogen, dislocations movements needs to lower stress levels. Considering the maximum value of C_{app} in the 800 W sample, it could be expected that the minimum energy for kink formation and the highest shielding effect belonged to 800 W. Thus, the maximum numbers of kinks could form in 800 W and cause further dislocation movement; thus, the yield stress in 800 W-C decreased. In other samples, as could be seen in Table 6, due to hydrogen charging, Ys increased and hydrogen hardening is observed. With decreasing trapped hydrogen in reversible sites, the required energy for kink formation increased and probably enough kinks were not formed on screw dislocations and also the shielding effect of hydrogen decreased. Thus, dislocation pile up and tangle could occur consequently hydrogen-induced hardening was observed [65–69].

Based on Table 6, the trend of changes in UTS is similar to Ys. In other words, in the 800 W sample, with hydrogen charging, UTS decreased while in other samples, it increased. Reduction of UTS in 800 W could be attributed to the minimum value of D_{app} which could restrict the extraction of hydrogen from reversible traps. This could keep elastic shielding effect and hold the required energy for the formation of kinks low. Also, the formed kinks and elastic shield may facilitate dislocation movement where finally UTS decreased in the 800 W sample. With increasing D_{app}, the extraction rate of hydrogen atoms and the energy required for kink formation increased and shielding effect decreased. Thus, UTS changes similar to D_{app} as below:

860 A, TMCP ˃ 60 A ˃ 800 W.

As the maximum value of D_{app} belonged to TMCP and 860 A samples, it seems that the maximum increase in UTS is attributed to 860 A and TMCP samples. Since, C_{app} in 860 A was lower than in TMCP, the energy required for kink formation in 860 A could be higher than in TMCP; and also shielding effect is lower in comparison to TMCP consequently, the number of kinks in 860 A could be lower than in TMCP. Thus, the value of UTS is higher in 860 A than in TMCP.

At the fracture surfaces of all charged samples, as shown with arrows in Fig. 7b, d, f, h, in addition to dimples, flat surfaces, and chevron marks can be observed with the characteristics of brittle fracture. In fracture surfaces of all reference samples (Fig. 7a, c, e, g), dimples could be seen. The atomic trapped hydrogens could combine and form hydrogen molecules in the interfaces of precipitation with matrix where the produced pressure could facilitate decohesion of precipitations; thus, failure could be obtained at lower strains where the dimple dimensions and their volume fractions decreased. Based on microscopic observations, it can be concluded that due to hydrogen, the fracture type changed from ductile to quasi cleavage. Other researchers also reported quasi-cleavage fracture due to the presence of hydrogen [70–72].

As shown in Fig. 11, the highest fracture toughness (K_{IC}) and fracture energy (G) is attributed to TMCP sample, and the lowest belongs to 60 A sample. It seems that the M/A micro constituents in the microstructure of 60 A, could result in minimizing K_{IC} and G. Also, another study reported that the presence of M/A micro constituents resulted in degradation of fracture toughness [70]. K_{IC} and G of 800 W were about 5% lower than those of TMCP. It seems that the presence of about 10% bainite in the 800 W microstructure could lead to greater toughness and fracture energy in this sample thatn it was expected. Other researchers have also reported the positive effect of bainite on fracture toughness [6, 72]. On the other hand, the toughness and fracture energy of 860 A sample were about 11% lower than those of TMCP. It seems that decreasing of DP percent and omission of thermomechanical effects due to heat treatment, resulted in diminished toughness and fracture energy in the 860 A sample. The trend of changes in K_{IC} and G in the charged samples (Fig. 12) can be attributed to the C_{app} trend. With elevation of C_{app}, more hydrogen embrittlement mechanisms could be activated and thus greater reductions in G and K_{IC} were obtained. It can be concluded that according to the extent of reduction in the fracture energy and toughness due to hydrogen, the microstructure consisting of M + B + F attributed to 800 W is the most susceptible to hydrogen embrittlement, while 860 A sample with the microstructure of F + MA + DP had the lowest susceptibility.

5 Conclusions

This research examined the influence of microstructure on the mechanical properties and fracture toughness of API X65 in the presence of hydrogen. Various heat treatments were carried out on TMCP as-received sample to obtain different microstructures. In order to measure the value of uptake and trapped hydrogen in the samples, Devanathanstachurski cell was fabricated. Tensile test was used to study the mechanical properties of reference and hydrogen charged samples. Note that in-situ hydrogen charging was performed during the tensile test along with hydrogen pre-charging.

Finally, using the indentation method, the fracture toughness values of references and pre-charged samples were measured. The results of this study can be summarized as follows:

(1) M + B + F microstructure had the minimum D_{app} and maximum C_{app} due to the highest density of reversible traps. On the other hand, in other microstructures, with the reduction of volume fractions of MA ` DP, C_{app} decreased while D_{app} increased.

(2) With hydrogen charging in the microstructure of M + B + F, the yield stress and UTS diminished. On the other hand, in the microstructure composed of ferrite (F), degenerated perlite (DP), and M/A micro constituent, YS and UTS increased.

(3) Hydrogen charging operation resulted in diminished elongation (El), reduction of area (RA), and ductile fracture percentage in all microstructures. Due to the presence of M, the microstructural combination of M + B + F had the maximum reduction.

(4) Hydrogen charging changed the fracture morphology from ductile to quasi-cleavage. Meanwhile, dimple dimensions and their volume percentages also decreased in the presence of hydrogen.

(5) With hydrogen pre-charging, for all microstructures, fracture toughness (K_{IC}) and fracture energy (G) decreased. The maximum K_{IC} and G were attributed to the microstructure obtained by thermomechanical operation while the minimum K_{IC} and G belonged to the M + B + F microstructure.

(6) M + B + F microstructure was the most susceptible to hydrogen embrittlement while the microstructure of F + MA + DP had the lowest susceptibility.

References

1. R. Wang, Corros. Sci. **51**(12), 2803 (2009)
2. H. Asahi, D. Hirakami, S. Yamasaki, ISIJ Int. **43**(4), 527 (2003)
3. D. Hejazi, A.J. Haq, N. Yazdipour, D.P. Dunne, A. Calka, F. Barbaro, E.V. Pereloma, Mat. Sci. Eng. A **551**, 40 (2012)
4. G.T. Park, S.U. Koh, H.G. Jung, K.Y. Kim, Corros. Sci. **50**(7), 1865 (2008)
5. B. Beidokhti, A. Dolati, A.H. Koukabi, Mat. Sci. Eng. A **507**(1–2), 167 (2009)
6. L. Tau, S.L.I. Chan, C.S. Shin, Corros. Sci. **38**(11), 2049 (1996)
7. F. Huang, J. Liu, Z.J. Deng, J.H. Cheng, Z.H. Lu, X.G. Li, Mat. Sci. Eng. A **527**(26), 6997 (2010)
8. T.S. Byun, J.W. Kim, J.H. Hong, J. Nucl. Mater. **252**(3), 187 (1998)
9. H. Miyazaki, H. Hyuga, K. Hirao, T. Ohji, J. Eur. Ceram. Soc. **27**(6), 2347 (2007)
10. T. Zhang, Y. Feng, R. Yang, P. Jiang, Scripta Mater. **62**(4), 199 (2010)
11. K.L. Murty, M.D. Mathew, Y. Wang, V.N. Shah, F.M. Haggag, Int. J. Pres. Ves. Pip. **75**(11), 831 (1998)
12. F. Yu, P. Y. Ben Jar, M.T. Hendry, in *Proceedings of the 2018 Joint Rail Conference*. 2018 Joint Rail Conference. Pittsburgh, Pennsylvania, USA. 18–20 April, 2018. Ball Indentation Technique to Estimate Fracture Toughness of High-Strength Rail Steels. (ASME, New York, 2018), p. V001T02A002
13. J.-S. Lee, J.-I. Jang, B.-W. Lee, Y. Choi, S.G. Lee, D. Kwon, Acta Mater. **54**(4), 1101 (2006)
14. M. He, F. Li, J. Cai, B. Chen, Theor. Appl. Fract. Mec. **56**(2), 104 (2011)
15. S.-W. Jeon, K.-W. Lee, J.Y. Kim, W.J. Kim, C.-P. Park, D. Kwon, Exp. Mech. **57**(7), 1013 (2017)
16. M.B. Bakirov, E.M. Morozov, I.A. Belunik, E.S. Krutko, Inorg. Mater. **51**(15), 1468 (2015)
17. J.-S. Lee, J.-I. Jang, K.-B. Yoo, D. Kwon, Key Eng. Mater. **321–323**, 480 (2006)
18. H. Zakerinia, A. Kermanpur, A. Najafizadeh, Int. J. ISSI **6**(10), 14 (2009)
19. M.A.V. Devanathan, Z. Stachurski, J. Electrochem. Soc. **111**(5), 619 (1964)
20. S.J. Kim, K.Y. Kim, Scripta Mater. **66**(12), 1069 (2012)
21. S.H. Wang, W.C. Luu, K.F. Ho, J.K. Wu, Mater. Chem. Phys. **77**(2), 447 (2003)
22. K. Banerjee, U.K. Chatterjee, Scripta Mater. **44**(2), 213 (2001)
23. S.K. Yen, I.B. Huang, Corrosion **59**(11), 995 (2003)
24. J. Gong, H. Miao, Z. Peng, Mater. Lett. **58**(7-8), 1349 (2004)
25. G.M. Pharr, Mat. Sci. Eng. A **253**(1-2), 151 (1998)
26. S. Zügner, K. Marquardt, I. Zimmermann, Eur. J. Pharm. Biopharm. **62**(2), 194 (2006)
27. W.C. Oliver, G.M. Pharr, J. Mater. Res. **19**(1), 3 (2004)
28. G.C. Sih, *A Special Theory of Crack Propagation. Mechanics of Fracture Initiation and Propagation* (Springer, Dordrecht, 1991), pp. 1–22
29. G.C. Sih, E.P. Chen, Theor. Appl. Fract. Mech. **40**(1), 1 (2003)
30. L.M. Kachanov, *Introduction to continuum damage mechanics* (Martinus Nijhoff Publisher, Leiden, 1986), p. 135
31. J. Lemaitre, J. Dufailly, Eng. Fract. Mech. **28**(5-6), 643 (1987)
32. C.Y. Tang, W.H. Tai, J. Mater. Process. Technol. **99**(1-3), 135 (2000)
33. M. He, F. Li, N. Ali, Mat. Sci. Eng. A **528**(3), 832 (2011)
34. H. Andersson, J. Mech. Phys. Solids **25**(3), 217 (1977)
35. A.L. Gurson, J. Eng. Mater. Technol. **99**(1), 2 (1977)
36. M.A. Arafin, J.A. Szpunar, Mat. Sci. Eng. A **528**(15), 4927 (2011)
37. S. Zajac, V. Schwinn, K.H. Tacke, Mater. Sci. Forum **500–501**, 387 (2005)
38. R. de Araujo Silva, L.F.G. de Souza, E. Valencia Morales, P.R. Rios, I. de Souza Bott, Mater. Res. **18**(5), 908 (2015)
39. V.V. Svishchenko, D.P. Cheprasov, O.V. Antonyuk, Met. Sci. Heat Treat. **46**(7-8), 324 (2004)
40. Li Wang, J.G. Speer, Microstruct. Anal. **2**(4), 268 (2013)
41. M. Masoumia, C.C. Silva, M. Béreš, D.H. Ladino, H.F.G. de Abreu, Int. J. Hydrog. Energy **42**(2), 1318 (2017)
42. R. Valentini, A. Solina, S. Matera, P. De Gregorio, Metallurg. Mater. Trans. A **27**(12), 3773 (1996)
43. A.J. Haq, K. Muzaka, D.P. Dunne, A. Calka, E.V. Pereloma, Int. J. Hydrog. Energy **38**(5), 2544 (2013)
44. A. Turnbull, M.W. Carroll, Corros. Sci. **30**(6-7), 667 (1990)
45. J.-Y. Lee, S.M. Lee, Surf. Coat. Technol. **28**(3–4), 301 (1986)
46. W.K. Kim, S.U. Koh, B.Y. Yang, K.Y. Kim, Corros. Sci. **50**(12), 3336 (2008)
47. E. Fallahmohammadi, F. Bolzoni, G. Fumagalli, G. Benassi, L. Lazzari, Int. J. Hydrog. Energy **39**(25), 13300 (2014)
48. L. Scoppio, M. Barteri, in *Hydrogen Transport and Cracking in Metals*, ed. by A. Turnbull. Proceedings of a Conference Held at the National Physical Laboratory, Teddington, 13-14 April 1994. Methods of hydrogen uptake measurements by electrochemical

permeation test on low alloy steels. (The Institute of Materials, London, 1995) p. 204

49. M.-C. Zhao, B. Tang, Y.-Y. Shan, K. Yang, Metall. Mater. Trans. A **34**(5), 1089 (2003)

50. P. Siahpour, R. Miresmaeili, A.S. Rouhaghdam, T. Indian I. Metals **71**(6), 1531 (2018)

51. E.V. Chatzidouros, V.J. Papazoglou, D.I. Pantelis, in *ASME 2011 30th International Conference on Ocean, Offshore and Arctic Engineering*. OMAE2011, Rotterdam, June 19–24, 2011. Hydrogen effect on fracture toughness of API 5L X70, X65 and X52 pipeline steel welds: an overview. vol. 3 (ASME, New York, 2011) p. 251

52. J. Capelle, J. Gilgert, G. Pluvinage, *Hydrogen Effect on Fatigue and Fracture of Pipe Steels* (Metz, Ecole Nationale d'Ingénieurs de Metz, 2009), pp. 8–10

53. S.-I. Komazaki, A. Koyama, T. Misawa, Mater. Trans. **43**(9), 2213 (2002)

54. T. Yokota, T. Shiraga, ISIJ Int. **43**(4), 534 (2003)

55. F.-G. Wei, T. Hara, T. Tsuchida, K. Tsuzaki, ISIJ Int. **43**(4), 539 (2003)

56. Y. Huang, A. Nakajima, A. Nishikata, T. Tsuru, ISIJ Int. **43**(4), 548 (2003)

57. E. Villalba, A. Atrens, Eng. Fail. Anal. **16**(1), 164 (2009)

58. G.M. Pressouyre, I.M. Bernstein, Corros. Sci. **18**(9), 819 (1978)

59. M.F. Stevens, I.M. Bernstein, Metall. Trans. A **20**(5), 909 (1989)

60. V. Kuzucu, M. Aksoy, M.H. Korkut, J. Mater. Process. Technol. **82**(1-3), 165 (1998)

61. S. Kang, Y.-S. Jung, J.-H. Jun, Y.-K. Lee, Mat. Sci. Eng. A **527**(3), 745 (2010)

62. S. Asher, P.M. Singh, in *NACE - International Corrosion Conference Series*, Corrosion 2008, New Orleans, March 16-20, 2008. Hydrogen Production and Permeation In Near-Neutral pH Environments (NACE International, Houston, 2008), pp. 084111-0841119

63. R. Kirchheim, Scripta Mater. **67**(9), 767 (2012)

64. H. Yu, A. Cocks, E. Tarleton, J. Mech. Phys. Solids **123**, 41 (2019)

65. M.B. Djukic, G.M. Bakic, V.S. Zeravcic, A. Sedmak, B. Rajicic, Eng. Fract. Mech. **216**, 106528 (2019)

66. M.L. Martin, M. Dadfarnia, A. Nagao, S. Wang, P. Sofronis, Acta Mater. **165**, 734 (2019)

67. A. Tehranchi, B. Yin, W.A. Curtin, Philos. Mag. **97**(6), 400 (2017)

68. R.K. Davani, R.M. Zadeh, M. Soltanmohammadi, Mat. Sci. Eng. A **718**, 135 (2018)

69. Q. Deng, W. Zhao, W. Jiang, T. Zhang, T. Li, Y. Zhao, J. Mater. Eng. Perform. **27**(4), 1654 (2018)

70. N. Huda, A.R.H. Midawi, J. Gianetto, R. Lazor, A.P. Gerlich, Mat. Sci. Eng. A **662**, 481 (2016)

71. A. Kumar, A. Singh, Mat. Sci. Eng. A **729**, 439 (2018)

72. H.A. glan, Z.Y. Liu, M.F. Hassan, M. Fateh, J. Mater. Process. Technol. **151**(1-3), 268 (2004)